

First-principles insights into all-optical spin switching in the half-metallic Heusler ferrimagnet Mn_2RuGa

G. P. Zhang*

Department of Physics, Indiana State University, Terre Haute, IN 47809, USA

Y. H. Bai

Office of Information Technology, Indiana State University, Terre Haute, IN 47809, USA

M. S. Si

*School of Materials and Engineering,
Lanzhou University, Lanzhou 730000, China*

Thomas F. George

*Departments of Chemistry & Biochemistry and Physics & Astronomy
University of Missouri-St. Louis, St. Louis, MO 63121, USA*

(Dated: July 22, 2022)

arXiv:2207.10443v1 [cond-mat.mtrl-sci] 21 Jul 2022

Abstract

All-optical spin switching (AOS) represents a new frontier in magnetic storage technology – spin manipulation without a magnetic field, – but its underlying working principle is not well understood. Many AOS ferrimagnets such as GdFeCo are amorphous and renders the high-level first-principles study unfeasible. The crystalline half-metallic Heusler Mn_2RuGa presents an opportunity. Here we carry out hitherto the comprehensive density functional investigation into the material properties of Mn_2RuGa , and introduce two concepts - the spin anchor site and the optical active site - as two pillars for AOS in ferrimagnets. In Mn_2RuGa , $\text{Mn}(4a)$ serves as the spin anchor site, whose band structure is below the Fermi level and has a strong spin moment, while $\text{Mn}(4c)$ is the optical active site whose band crosses the Fermi level. Our magneto-optical Kerr spectrum and band structure calculation jointly reveal that the delicate competition between the Ru-4*d* and Ga-4*p* states is responsible for the creation of these two sites. These two sites found here not only present a unified picture for both Mn_2RuGa and GdFeCo, but also open the door for the future applications. Specifically, we propose a $\text{Mn}_2\text{Ru}_x\text{Ga}$ -based magnetic tunnel junction where a single laser pulse can control magnetoresistance.

PACS numbers:

Keywords:

I. INTRODUCTION

Laser-induced ultrafast demagnetization¹ changes the landscape of spin manipulation, where the laser field plays a central role in magnetism. All-optical spin switching (AOS)² is a prime example, where a single laser pulse can turn spins from one direction to another, free of an external magnetic field. As more and more materials are discovered³⁻⁵, a critical question on the horizon is what properties are essential to AOS. Earlier studies have focused on magnetic orderings such as ferrimagnetic versus ferromagnetic⁶, sample composition⁷, compensation temperature⁸, magnetic domains⁹ and others¹⁰, but most AOS materials are amorphous and difficult to simulate within state-of-the-art density functional theory. This greatly hampers the current effort to decipher the mystery of AOS at a microscopical level that goes beyond the existing phenomenological understanding¹¹.

Heusler compounds represent a new opportunity^{12,13}. Their properties can be systematically tailored, only subject to the structure stability. Different from rare-earth-transition metals^{2,14}, one has an empirical Slater-Pauling rule to predict spin moments¹⁵⁻²². Although this rule is simple²³, the actual synthesis of a desired material is a monumental task of decades in making²⁴, because many materials are unstable experimentally. In 2002, Hori *et al.*²⁵ successfully synthesized various $(\text{Mn}_{1-x}\text{Ru}_x)_3\text{Ga}$ alloys with $x = 0.33 - 0.67$ and determined the spin moment of $1.15 \mu_B$ per formula. In 2014, Kurt *et al.*²⁶ demonstrated that Ru can significantly reduce the spin moment in ferrimagnet $\text{Mn}_2\text{Ru}_x\text{Ga}$. Because one can tune composition x , $\text{Mn}_2\text{Ru}_x\text{Ga}$ is likely to be a half-metal and fully-compensated ferrimagnet^{27,28}, with no stray field, ideal for spintronics^{13,29,30}. Research has intensified immediately^{21,31-35}. Lenne *et al.*³⁶ found that the spin-orbit torque reaches $10^{-11}\text{Tm}^2/\text{A}$ in the low-current limit. Banerjee *et al.*³⁷ reported that a single 200-fs/800-nm laser pulse can toggle the spin from one direction to another in Mn_2RuGa within 2 ps or less. Just as found in GdFeCo ^{2,11}, for every consecutive pulse, the spin direction is switched. This discovery³⁷ demonstrates the extraordinary tunability of Heusler compounds, which now changes the trajectory of AOS research³⁸⁻⁴⁰, with Mn_2RuGa as a crystalline model system where the first-principles investigation is now possible.

In this paper, we carry out the comprehensive first-principles density-functional study to pin down the material properties essential to all-optical-spin switching in ferrimagnet Mn_2RuGa . We introduce two concepts - the spin anchor site (SAS) and the optical active

site (OAS) as two essential pillars of AOS in ferrimagnets. SAS has a strong spin moment, and in Mn_2RuGa it is the $\text{Mn}(4a)$ site. Our band structure reveals that the $\text{Mn}(4a)$'s band is 0.5 eV below the Fermi level. By contrast, OAS has a smaller spin moment, easier to be switched optically⁴¹, and in Mn_2RuGa it is the $\text{Mn}(4c)$ site. Its band is around the Fermi level and accessible to optical excitation⁴². The creation of SAS and OAS is the making of Ru and Ga. The Ru-4*d* electrons set up the initial spin configuration with a strong spin moment concentrated on the distant $\text{Mn}(4c)$, but Ga tips this balance and reverses the relative spin magnitude between $\text{Mn}(4a)$ and $\text{Mn}(4c)$. Although Ru and Ga are weakly magnetic, their energy bands appear in the same energy window as two Mn atoms, which is manifested in the magneto-optical Kerr spectrum. Guided by two essential sites, we can now unify Mn_2RuGa with GdFeCo , despite of their apparent structural differences, and extract three essential properties for AOS. (i) A ferrimagnet must have a spin anchor site, i.e. Gd in GdFeCo and $\text{Mn}(4a)$ in Mn_2RuGa . (ii) It must have an optical active site, i.e. Fe in GdFeCo and $\text{Mn}_2(4c)$ in Mn_2RuGa . (iii) Its spin anchor site and optical active site must be antiferromagnetically coupled to minimize the potential energy barrier⁴³. We propose a laser-activated magnetic tunnel junction based on the same material $\text{Mn}_2\text{Ru}_x\text{Ga}$, but with different compositions x which form optical activation, spin filtering and reference layers. This device, if successful, represents an ideal integration of fully-compensated half-metallicity in spintronics into all-optical spin switching in femtomagnetism^{44,45}.

The rest of the paper is arranged as follows. In Sec. II, we present our theoretical formalism. Section III is devoted to the results and discussion, which includes the crystal structure, electronic band structure, ultrafast demagnetization, and Kerr rotation angle. Finally, we conclude this paper in Sec. IV.

II. THEORETICAL FORMALISM AND CALCULATION

Element Mn lies in the middle of 3*d* transition metals, with a half-filled 3*d* shell and zero orbital moment, just as Gd in the middle of 4*f* rare-earth metals. Mn is the only 3*d* transition metal element in inverse Heusler compounds, which is similar to a rare-earth element⁴⁶. Mn_2RuGa crystallizes in an inverse *XA* Heusler structure^{21,22,31,35,46} (see Fig. 1(a)), where two manganese atoms, Mn_1 and Mn_2 , are situated at two distinct Wyckoff positions $4a(0, 0, 0)$ and $4c(\frac{1}{4}, \frac{1}{4}, \frac{1}{4})$, and are antiferromagnetically coupled. Ru and Ga sit at

$4d(\frac{3}{4}, \frac{3}{4}, \frac{3}{4})$ and $4b(\frac{1}{2}, \frac{1}{2}, \frac{1}{2})$, respectively. The inverse Heusler XA structure has two Mn atoms separated by a vector $(\frac{1}{4}, \frac{1}{4}, \frac{1}{4})$, while the $L2_1$ structure by $(\frac{1}{2}, \frac{1}{2}, \frac{1}{2})$ ^{26,32,33}. The experimental lattice constants in this nearly cubic material are $a = b = c = 5.97\text{\AA}$ ²⁶. Viewing along the diagonal direction, four atoms form chains $\text{Mn}_1\text{-Mn}_2\text{-Ga-Ru-Mn}_1 \dots$. Therefore, Mn_2RuGa loses both inversion and time reversal symmetries due to the antiferromagnetic coupling between two Mn atoms.

We employ the state-of-the-art density functional theory and the full-potential linearized augmented plane wave (FLAPW), as implemented in the Wien2k code⁴⁷. We first self-consistently solve the Kohn-Sham equation

$$\left[-\frac{\hbar^2 \nabla^2}{2m_e} + V_{Ne} + V_H + V_{xc} \right] \psi_{n\mathbf{k}}(r) = E_{n\mathbf{k}} \psi_{n\mathbf{k}}(r), \quad (1)$$

where $\psi_{n\mathbf{k}}(r)$ is the wavefunction of band n at the crystal momentum \mathbf{k} and $E_{n\mathbf{k}}$ is its band energy. The terms on the left are the kinetic energy operator, the attraction between the nuclei and electrons, the Hartree term, and the exchange-correlation⁴⁸, respectively. The spin-orbit coupling is included using a second-variational method in the same self-consistent iteration.

III. RESULTS AND DISCUSSIONS

A. Crystal structure

Ordered Heusler alloys have three distinctive kinds of structures⁴⁹: (1) normal full-Heusler X_2YZ alloys with group symmetry $L2_1$, (2) half Heusler XYZ compounds with group symmetry $C1_b$, and (3) inverse Heusler X_2YZ alloys with group symmetry XA . (1) has the space group No. 225. (2) and (3) have the same space group No. 216. $L2_1$ has (8c) site, which is split into two different sites in XA ⁴⁶. However, over the years, various Wyckoff positions are adopted in the literature. For the XA structure, Wollmann *et al.*⁴⁶ used a different set of Wyckoff positions for Mn at $4d(\frac{1}{4}, \frac{1}{4}, \frac{1}{4})$, Y at $4c(\frac{3}{4}, \frac{3}{4}, \frac{3}{4})$, Mn at $4b(\frac{1}{2}, \frac{1}{2}, \frac{1}{2})$, and Z at $4a(0, 0, 0)$. So in their paper, their (4a), (4b), (4c), (4d) positions have different meanings from those in³¹. In order to convert Wollmann's notation to the latter notation, one has to shift the entire cell by $4d(\frac{1}{4}, \frac{1}{4}, \frac{1}{4})$. For the $L2_1$ structure, Wollmann *et al.*⁴⁶ also adopted different positions, which were again used in their review paper¹³ (see Table I).

In Mn_2RuGa , several versions have also been used. It adopts an XA structure. Kurt *et al.*²⁶ correctly assigned the space group symmetry $L2_1$ to the full Heusler compound, but inappropriately assigned the same group to Mn_2RuGa , and so did Zic *et al.*³². Both Zic *et al.*³² and Fleischer *et al.*³³ had the correct notations for all the atoms, but their figure switched the positions for Ru and Mn_2 , where Ru($4d$) appears at position $4c(\frac{1}{4}, \frac{1}{4}, \frac{1}{4})$ and $\text{Mn}_2(4c)$ at $4d(\frac{3}{4}, \frac{3}{4}, \frac{3}{4})$. Since they never used the figure to characterize their experimental data, this change does not affect their results. We also notice that Betto *et al.*⁵⁰ assigned $C1_b$ group symmetry to Mn_2RuGa , where two Mn atoms are at $4a(0, 0, 0)$ and $4c(3/4, 3/4, 3/4)$ while Ru at $4d(1/4, 1/4, 1/4)$ and Ga at $4b(1/2, 1/2, 1/2)$. One can see from Table I that $C1_b$ has no $4c$ site.

Galanakis *et al.*³¹ exchanged the positions for Ru and Ga, so Ru is at site $4b$ and Ga is at site $4d$. Although in general such an exchange is allowed, they do not match the existing experimental results⁴². For instance, only $\text{Mn}_1(4a)$ has Ru as its neighbor. If we exchange the positions for Ru and Ga, then $\text{Mn}_2(4c)$ would have Ru as its neighbor.

We summarize those used Wyckoff positions in the same table, so the reader can see the difference. We adopt the common convention, as listed in the last line in Table I. This convention matches the experimental results better³³. In particular, the magneto-optics signal agrees with the experimental one.

B. Band structure

We choose a big k mesh of $44 \times 44 \times 44$, with 11166 irreducible k points in the Brillouin zone. The product of the Muffin-tin radius R_{MT} and the planewave cutoff is 7, where $R_{\text{MT}}(\text{Mn}_1, \text{Mn}_2, \text{Ru}) = 2.42$ bohr, and $R_{\text{MT}}(\text{Ga}) = 2.28$ bohr. We find that Mn_1 has spin moment of $M_{4a} = 3.17\mu_{\text{B}}$. We call $\text{Mn}_1(4a)$ the spin anchor site, SAS, as it pins the magnetic configuration, so the magnetic structure can be stabilized and is immune to optical excitation. $\text{Mn}_2(4c)$ atoms form another spin sublattice with a smaller spin moment of $-M_{4c} = -2.31\mu_{\text{B}}$. The entire cell has the spin moment of $1.027 \mu_{\text{B}}$, in agreement with prior studies^{21,31}. Figure 1(a) shows the spatial valence spin density integrated from 2 eV below the Fermi level for each atom, where the red(blue) color refers to the majority(minority) spin. One can see the spin density is mainly localized on these two Mn atoms, where Mn_1 has a larger spin in the spin up channel and Mn_2 has the spin density in the spin down

channel, so they are antiferromagnetically coupled.

Our first finding is that the above spin configuration hinges on the delicate balance between Ru and Ga. Figure 1(b) shows their respective atomic energies. Ru's $4d^7 5s^1$ states are close to Mn's unoccupied $5d^0$ states. Without Ga, when Mn and Ru form a solid, the spin moment on Ru increases by five times to $0.39\mu_B$ and is antiferromagnetically coupled to the $\text{Mn}_1(4a)$'s spin, but its spin is now ferromagnetically coupled to the distant $\text{Mn}_2(4c)$, which is opposite to the native Mn_2RuGa (see Table II). Adding Ga tips the balance, because Ga's $4p^1$ is higher than Mn's unoccupied $5d^0$ orbitals (see Fig. 1(b)), so Ga can transfer electrons to Mn atoms more easily than Ru. We integrate the atom-resolved density of states around each sphere, and find that the number of the Ru $4d$ electrons is 5.87, reduced by 1.13 with respect to its atomic $4d^7$, while the $4p$ electron of Ga is 0.81, reduced by 0.2 from $4p^1$. The total number of electrons within the $\text{Mn}_1(4a)$ and $\text{Mn}_2(4c)$ spheres are almost exactly the same, 6.04, but the number of $3d$ electrons in each spin channel is very different. Table II shows that $\text{Mn}_1(4a)$ has 4.09 $3d$ electrons in the majority channel and 1.01 in the minority channel, in contrast to $\text{Mn}_2(4c)$ where 1.44 and 3.72 electrons are present. The total number of $3d$ electron is still close to 5. Table II summarizes these results. In general, the orbital moment on Mn_1 is small, around $0.025\mu_B$, and that on Mn_2 is slightly larger, reaching $-0.046\mu_B$, which is beneficial to the spin-orbit torque^{38,43}, important for AOS³⁷.

Figure 2(a) shows the band structure, superimposed with the Mn_1 - $3d$ orbital character from its spin majority channel. The orbital characters are highlighted by the circles, whose radius is proportional to the weight of the Mn_1 - $3d$ character, and the lines are the actual band dispersion. Bands with a clear dominance of a single orbital are highlighted, and in the figure, d_{z^2} and $d_{x^2-y^2}$ are denoted by z^2 and $x^2 - y^2$ for simplicity; and this is the same for other orbitals. The entire set of detailed orbital characterization is presented in⁵¹. We see that the Mn_1 's occupied majority band centers around -0.6 eV below the Fermi level E_F (horizontal dashed line), with a smaller contribution close to the Fermi level. This feature is reflected in the $3d$ -partial density of states (pDOS) in Fig. 2(b), where a small peak at the Fermi level is found, consistent with two prior studies^{21,31}, indicative of structural instability⁴⁶. Figure 2(c) shows that the Mn_1 spin minority band has a single d_{xz}/d_{yz} band, which crosses the Fermi level from the L to Γ , and then to X point, but this single band crossing does not constitute a major contribution to the density of states (DOS). Figure 2(d) shows the partial $3d$ density of states at the Fermi level is very tiny but not zero. The other

occupied minority d band is at -1.5 eV below the Fermi level. Because $\text{Mn}_1(4a)$'s d band is away from E_F and has a small density of states around the Fermi level, optical excitation at Mn_1 is weak⁴².

$\text{Mn}_2(4c)$ is quite different from $\text{Mn}_1(4a)$. Figure 2(f) shows that its majority bands cross the Fermi level at multiple points, have mixed d characters, and are highly dispersive. Its $3d$ -pDOS (Fig. 2(e)) has a larger peak at the Fermi level than Mn_1 , quantitatively 1.80-1.81 states/eV for the former and 0.65-0.69 states/eV for the latter. This explains why $\text{Mn}_2(4c)$ is more optically active than $\text{Mn}_1(4a)$ ⁴², where we call $\text{Mn}_2(4c)$ the optical active site. In the minority channel, Mn_2 has a strong admixture of orbital characters (see Fig. 2(h)), and its overall density of states at the Fermi level is also small (see Fig. 2(g)). We note that the minority band structure is very similar to that of Mn_3Ga ¹⁶, and they both have a flat d_{z^2} band along the Γ -X direction.

Before we move on to ultrafast demagnetization, we must emphasize that the band structure is not solely contributed by these two Mn atoms. Both Ru and Ga significantly affect the magnetic properties of Mn atoms. Thin lines in Figs. 2(e) and 2(g) are the Ru's $4d$ pDOS for the spin majority and minority channels, respectively. One can see that the Ru- d majority density of states follows the $\text{Mn}_1(4a)$'s pDOS (compare Figs. 2(b) and (e)), but its minority state follows the $\text{Mn}_2(4c)$'s pDOS (compare the thin and thick lines in Fig. 2(g)). The split role from the same atom is remarkable.

C. Ultrafast demagnetization

The circles in Fig. 3(a) are the experimental ultrafast demagnetization⁴², and consist of two regions. Region I is from 0 to 0.26 ps, highlighted by the red arrow in Fig. 3(a), and region II starts from 0.26 ps to 5 ps. This time separation of 0.26 ps is consistent with a prior study⁵². In region I, a sharp decrease in spin moment is observed, but in region II there is a peak. We can fit these two regions with the same equation,

$$\frac{\Delta M(t)}{M} = A \left(\frac{M_{4a}e^{-\alpha_{4a}(t-\mathcal{T})} - M_{4c}e^{-\alpha_{4c}(t-\mathcal{T})}}{M_{4a} - M_{4c}} \right) - B, \quad (2)$$

where t is the time. A is necessary, since without it the laser field amplitude cannot enter the equation. B determines the net amount of demagnetization. \mathcal{T} sets the characteristic time for demagnetization or remagnetization. Since our spin moments are fixed by our calculation,

we only have four fitting parameters for each region, where $\alpha_{4a(4c)}$ is the demagnetization rate for site $4a(4c)$. Table II shows that in region I, α is site-dependent, $\alpha_{4a} = 4.5/\text{ps}$ and $\alpha_{4c} = 2.8/\text{ps}$, demonstrating that the larger the spin moment is, the larger α becomes,

$$\alpha = cM, \text{ or, } \tau_M = \frac{1}{cM}, \quad (3)$$

where c is a constant. This equation is consistent with the empirical formula proposed by Koopmans and coworkers⁵³. From α , we find the demagnetization times $\tau_M(4a) = 222$ fs, and $\tau_M(4c) = 357$ fs. These intrinsic demagnetization times, called the Hübner times¹⁰, are well within the times for other transition and rare-earth metals: 58.9 fs (Fe), 176 fs (Ni), 363 fs [Gd($5d$)], 690 fs [Gd($4f$)]. An extreme point will appear if $\partial \left(\frac{\Delta M(t)}{M} \right) / \partial t = 0$, and the second-order time-derivative determines whether the extreme is a maximum or minimum,

$$\frac{\partial^2 \left(\frac{\Delta M(t)}{M} \right)}{\partial t^2} = A\alpha_{4c}M_{4c}e^{-\alpha_{4c}(t-T)}(\alpha_{4a} - \alpha_{4c}). \quad (4)$$

If $\alpha_{4a} > \alpha_{4c}$, we only have a minimum which explains the spin change in region I. In region II, both α_{4a} and α_{4c} are reduced, but α_{4a} is reduced much more, so $\alpha_{4a} < \alpha_{4c}$, which corresponds to a peak in region II. Table II shows that region II has $\alpha_{4a} = 0.6/\text{ps}$ and $\alpha_{4c} = 1.5/\text{ps}$. The demagnetization on the $4a$ site slows down significantly.

D. Kerr rotation angle

Underlying ultrafast demagnetization and subsequent all-optical spin switching is the magneto-optical property of Mn_2RuGa , which is characterized by the conductivity⁵⁴ in units of $(\Omega\text{m})^{-1}$,

$$\sigma_{\alpha\beta}(\omega) = \frac{i\hbar e^2}{m_e^2 V} \sum_{k;m,n} \frac{f_{nk} - f_{mk}}{E_{mk} - E_{nk}} \frac{\langle nk|p_\alpha|mk\rangle \langle mk|p_\beta|nk\rangle}{(\hbar\omega + i\eta) + (E_{nk} - E_{mk})}, \quad (5)$$

where m_e is the electron mass, V is the unit cell volume, f_{nk} is the Fermi distribution function, E_{mk} is the band energy of state $|mk\rangle$, $\langle nk|p_\alpha|mk\rangle$ is the momentum matrix element between states $|mk\rangle$ and $|nk\rangle$, and η is the damping parameter. The summation is over the crystal momentum k and all the band states $|mk\rangle$ and $|nk\rangle$, and ω is the incident photon frequency. Here α and β refer to the directions, such as the x and y directions, not to be confused with the above demagnetization rate. The anomalous Hall conductivity is just the off-diagonal term. In the limit of $\eta, \omega \rightarrow 0$, the term behind the summation over k is the

Berry curvature

$$\Omega_{\alpha,\beta}^{k,n} = \sum_{m \neq n} \hbar^2 \frac{(f_{mk} - f_{nk}) \langle nk | v_\alpha | mk \rangle \langle mk | v_\beta | nk \rangle}{(E_{mk} - E_{nk})^2}. \quad (6)$$

The general expression given in Eq. 5 is better suited for metals with partial occupation than the treatment with a separate sum over occupied and unoccupied states^{55,56}, though the latter is faster. The intraband transition with $n = m$ is included by replacing $(f_{nk} - f_{mk})/(E_{mk} - E_{nk})$ by its derivative $-\partial f_{nk}/\partial E_{nk}$, which is $-\frac{\beta/2}{\cosh \beta(E_{nk} - E_F) + 1}$, without resorting to more complicated numerics⁵⁷. Here $\beta = 1/(k_B T)$, where k_B is the Boltzmann constant, T is the temperature, and E_F is the Fermi energy. The Kerr effect is characterized by the Kerr rotation θ and ellipticity ϵ , in the small angle limit and with magnetization along the z axis,

$$\theta + i\epsilon = -\frac{\sigma_{xy}}{\sigma_{xx} \sqrt{1 + 4\pi i \sigma_{xx}/\omega}}, \quad (7)$$

where σ_{xx} must be converted to 1/s. The SI version of $\sqrt{1 + 4\pi i \sigma_{xx}/\omega}$ is $\sqrt{1 + i \sigma_{xx}/(\omega \epsilon_0)}$.

Experimentally, Fleischer *et al.*³³ measured the magneto-optical Kerr effect for a series of $\text{Mn}_2\text{Ru}_x\text{Ga}$ samples with compositions $x = 0.61, 0.62, 0.69, 0.83$ and with thickness from 26 to 81 nm. Figure 3(b) reproduces two sets of data from their supplementary materials. One can see that both the thickness and composition affect the Kerr rotation angle. The thicker sample has a larger angle (compare dotted and long-dashed lines with $x = 0.61, 0.62$), and the angle peaks between 1.6-1.9 eV. Our theoretical Kerr angles with three different dampings are three solid lines with $\eta = 0.8, 0.6$ and 0.4 eV from the bottom to top, respectively. One notices that the overall shape is similar to the experimental data, and the main peak is also around 2 eV, slightly higher than the experimental one, but a more direct comparison is not possible since there are no experimental data at $x = 1$. The best agreement in terms of the Kerr angle is obtained with $\eta = 0.8$ eV. The convergence of our spectrum is tested against the mesh of $92 \times 92 \times 92$, and there is no visual difference between this much bigger mesh and the one used in Fig. 3(b).

We can pinpoint the origin of the main peak by removing some atoms. We use $\eta = 0.4$ eV since it gives us more structures. First, we remove $\text{Mn}_2(4c)$, without changing the lattice structure and the rest of atoms, so we have $\text{Mn}(4a)\text{RuGa}$. The solid line in Fig. 3(c) shows that the Kerr rotation angle for the new $\text{Mn}(4a)\text{RuGa}$ is very different from the one in Fig. 3(b), highlighting the fact that $\text{Mn}_2(4c)$, not $\text{Mn}_1(4a)$, contributes significantly to the overall signal. To verify this, we remove $\text{Mn}_1(4a)$ but keep $\text{Mn}_2(4c)$. The red long-dashed

line shows clearly that the overall shape is well reproduced, but the Kerr angle is larger. This concludes that $\text{Mn}_2(4c)$ is optically active and plays a decisive role in the magneto-optical response as OAS, consistent with the experiment⁴², but the role of Ru and Ga should not be underestimated. Magnetically, they are silent and do not contribute to the spin moment significantly, but when we remove Ru, the spectrum changes completely (see the dotted line in Fig. 3(c)). The same thing happens to the removal of Ga atom. This reveals the significant contributions of Ru and Ga to the optical response of Mn_2RuGa . The discovery of two sites (spin anchor site and optical active site) found here has some resemblance to the laser-induced intersite spin transfer⁵⁸. In their system, Dewhurst *et al.* found that the spins of two Mn atoms are aligned and coupled ferromagnetically, not antiferromagnetically coupled as found here. Additional calculations are necessary since their materials are not Mn_2RuGa . Mentink *et al.*⁵⁹ proposed a two-sublattice spin model where AOS is realized through the angular momentum exchange between sublattices. But they did not reveal the different roles played by two spin sublattices. Our mechanism makes a clear distinction between two sublattices, and thus ensures that two sublattices do not compete optically and magnetically.

IV. CONCLUSION

Through Mn_2RuGa , our state-of-the-art first-principles density functional calculation establishes two concepts: the spin anchor site and the optical active site as the key to AOS in ferrimagnets. The formation of SAS and OAS in Mn_2RuGa is accomplished by weakly magnetic Ru and Ga atoms. In GdFeCo^2 Gd is SAS while Fe is OAS. Switching starts with OAS⁵²; because the ferrimagnetic coupling between SAS and OAS is frustrated and has a lower potential barrier to overcome if the spin moment is smaller⁶⁰, SAS is dragged into the opposite direction by OAS through the spin torque $J\mathbf{S}_i \times \mathbf{S}_j$ ^{38,41}, to realize all-optical spin switching. Because the Heusler compounds have excellent tunability^{13,17,19,22,29,33}, the future research can investigate the effect of the spin moments at SAS and OAS on the spin switchability⁸. We envision an integrated device based on Mn_2RuGa as illustrated in Fig. 1(c). All three parts of the device are made of the same materials but with different concentration x . In the middle, x is close to 0.6, so we have a full-compensated half-metal, while at two ends, x is close to 1, whose spin is designed to be optically switched. This forms an

ideal magnetic tunnel junction that a light pulse can activate. A future experimental test is necessary. We should add that experimentally, concentrations of both Mn and Ru can be already tuned in several different experimental groups. Chatterjee *et al.*³⁵ were able to adopt two concentrations $x = 0.2, 0.5$ in $\text{Mn}_{2-x}\text{Ru}_{1+x}$, while Siewierska *et al.*³⁴ were able to independently change x and y in $\text{Mn}_y\text{Ru}_x\text{Ga}$ films. In fact, Banerjee *et al.*³⁷ already used 13 samples with $x = 0.5$ up to 1.0 in $\text{Mn}_2\text{Ru}_x\text{Ga}$.

Acknowledgments

The authors appreciate the numerous communications with Dr. K. Rode (Dublin) and Dr. K. Fleischer (Dublin). Dr. Fleischer provided the original experimental data in text form, which is very convenient to plot, with a small correction to the thickness of their samples. G.P.Z. and Y.H.B. were supported by the U.S. Department of Energy under Contract No. DE-FG02-06ER46304. Part of the work was done on Indiana State University's high performance Quantum and Obsidian clusters. The research used resources of the National Energy Research Scientific Computing Center, which is supported by the Office of Science of the U.S. Department of Energy under Contract No. DE-AC02-05CH11231. M.S.S. was supported by the National Science Foundation of China under grant No. 11874189.

* guo-ping.zhang@outlook.com. <https://orcid.org/0000-0002-1792-2701>

-
- ¹ E. Beaurepaire, J. C. Merle, A. Daunois, and J.-Y. Bigot, Ultrafast spin dynamics in ferromagnetic nickel, *Phys. Rev. Lett.* **76**, 4250 (1996).
 - ² C. D. Stanciu, F. Hansteen, A. V. Kimel, A. Kirilyuk, A. Tsukamoto, A. Itoh, and Th. Rasing, All-optical magnetic recording with circularly polarized light, *Phys. Rev. Lett.* **99**, 047601 (2007).
 - ³ S. Mangin, M. Gottwald, C-H. Lambert, D. Steil, V. Uhler, L. Pang, M. Hehn, S. Alebrand, M. Cinchetti, G. Malinowski, Y. Fainman, M. Aeschlimann, and E. E. Fullerton, Engineered materials for all-optical helicity-dependent magnetic switching, *Nat. Mater.* **13**, 286 (2014).
 - ⁴ C.-H. Lambert, S. Mangin, B. S. D. Ch. S. Varaprasad, Y. K. Takahashi, M. Hehn, M. Cinchetti, G. Malinowski, K. Hono, Y. Fainman, M. Aeschlimann, and E. E. Fullerton, All-optical control

- of ferromagnetic thin films and nanostructures, *Science* **345**, 1337 (2014).
- ⁵ M. Vomir, M. Albrecht, and J.-Y. Bigot, Single shot all optical switching of intrinsic micron size magnetic domains of a Pt/Co/Pt ferromagnetic stack, *Appl. Phys. Lett.* **111**, 242404 (2017).
- ⁶ C. Schubert, A. Hassdenteufel, P. Matthes, J. Schmidt, M. Helm, R. Bratschitsch, and M. Albrecht, All-optical helicity dependent magnetic switching in an artificial zero moment magnet, *Appl. Phys. Lett.* **104**, 082406 (2014).
- ⁷ A. Hassdenteufel, J. Schmidt, C. Schubert, B. Hebler, M. Helm, M. Albrecht, and R. Bratschitsch, Low-remanence criterion for helicity-dependent all-optical magnetic switching in ferrimagnets, *Phys. Rev. B* **91**, 104431 (2015).
- ⁸ K. Vahaplar, A. M. Kalashnikova, A. V. Kimel, S. Gerlach, D. Hinzke, U. Nowak, R. Chantrell, A. Tsukamoto, A. Itoh, A. Kirilyuk, and Th. Rasing, All-optical magnetization reversal by circularly polarized laser pulses: Experiment and multiscale modeling, *Phys. Rev. B* **85**, 104402 (2012).
- ⁹ M. S. El Hadri, P. Pirro, C.-H. Lambert, S. Petit-Watelot, Y. Quessab, M. Hehn, F. Montaigne, G. Malinowski, and S. Mangin, Two types of all-optical magnetization switching mechanisms using femtosecond laser pulses, *Phys. Rev. B* **94**, 064412 (2016).
- ¹⁰ G. P. Zhang, G. Lefkidis, M. Murakami, W. Hübner, and T. F. George, *Introduction to Ultrafast Phenomena: From Femtosecond Magnetism to High-Harmonic Generation*, CRC Press, Taylor & Francis Group, Boca Raton, Florida (2021).
- ¹¹ T. A. Ostler, J. Barker, R. F. L. Evans, R. W. Chantrell, U. Atxitia, O. Chubykalo-Fesenko, S. El Moussaoui, L. Le Guyader, E. Mengotti, L. J. Heyderman, F. Nolting, A. Tsukamoto, A. Itoh, D. Afanasiev, B. A. Ivanov, A. M. Kalashnikova, K. Vahaplar, J. Mentink, A. Kirilyuk, Th. Rasing, and A. V. Kimel, Ultrafast heating as a sufficient stimulus for magnetization reversal in a ferrimagnet, *Nat. Commun.* **3**, 666 (2012).
- ¹² I. Galanakis, P. H. Dederichs, and N. Papanikolaou, Origin and properties of the gap in the half-ferromagnetic Heusler alloys, *Phys. Rev. B* **66**, 134428 (2002).
- ¹³ L. Wollmann, A. K. Nayak, S. S. P. Parkin, and C. Felser, Heusler 4.0: Tunable Materials, *Annu. Rev. Mater. Res.* **47**, 247 (2017).
- ¹⁴ A. Hassdenteufel, B. Hebler, C. Schubert, A. Liebig, M. Teich, M. Helm, M. Aeschlimann, M. Albrecht, and R. Bratschitsch, Thermally assisted all-optical helicity dependent magnetic switching in amorphous $\text{Fe}_{100-x}\text{Tb}_x$ alloy films, *Adv. Mater.* **25**, 3122 (2013).

- ¹⁵ S. Wurmehl, G. H. Fecher, H. C. Kandpal, V. Ksenofontov, C. Felser, H.-J. Lin, and J. Morais, Geometric, electronic, and magnetic structure of Co_2FeSi : Curie temperature and magnetic moment measurements and calculations, *Phys. Rev. B* **72**, 184434 (2005).
- ¹⁶ S. Wurmehl, H. C. Kandpal, G. H. Fecher, and C. Felser, Valence electron rules for prediction of half-metallic compensated-ferrimagnetic behaviour of Heusler compounds with complete spin polarization, *J. Phys.: Condens. Matter* **18**, 6171 (2006).
- ¹⁷ G. D. Liu, X. F. Dai, S. Y. Yu, Z. Y. Zhu, J. L. Chen, G. H. Wu, H. Zhu, and J. Q. Xiao, Physical and electronic structure and magnetism of Mn_2NiGa : Experiment and density-functional theory calculations, *Phys. Rev. B* **74**, 054435 (2006).
- ¹⁸ L. Wollmann, S. Chadov, J. Kübler, and C. Felser, Magnetism in tetragonal manganese-rich Heusler compounds, *Phys. Rev. B* **92**, 064417 (2015).
- ¹⁹ T. Song, Q. Ma, X.-W. Sun, Z.-J. Liu, X.-P. Wei, and J.-H. Tian, High-pressure and high-temperature physical properties of half-metallic full-Heusler alloy Mn_2RuSi by first-principles and quasi-harmonic Debye model, *J. Mag. Mag. Mater.* **424**, 359 (2017).
- ²⁰ K. Z. Suzuki, Y. Miura, R. Ranjbar, L. Bainsla, A. Ono, Y. Sasaki, and S. Mizukami, Perpendicular magnetic tunnel junctions with Mn-modified ultrathin MnGa layer, *Appl. Phys. Lett.* **112**, 062402 (2018).
- ²¹ L. Yang, B. Liu, F. Meng, H. Liu, H. Luo, E. Liu, W. Wang and G. Wu, Magnetic properties of Heusler alloy Mn_2RuGe and Mn_2RuGa ribbons, *J. Mag. Magn. Mater.* **379**, 1 (2015).
- ²² W. Zhang, Y. Jin, R. Skomski, P. Kharel, X. Li, T. Chen, G. Zhao, D. Kim, S. Valloppilly, and D. J. Sellmyer, Mn_2CrGa -based Heusler alloys with low net moment and high spin polarization, *J. Phys. D: Appl. Phys.* **51**, 255001 (2018).
- ²³ H. van Leuken and R. A. de Groot, Half-Metallic Antiferromagnets, *Phys. Rev. Lett.* **74**, 1171 (1995).
- ²⁴ K. Rode, N. Baadji, D. Betto, Y.-C. Lau, H. Kurt, M. Venkatesan, P. Stamenov, S. Sanvito, J. M. D. Coey, E. Fonda, E. Otero, F. Choueikani, P. Ohresser, F. Porcher, and G. Andre, Site-specific order and magnetism in tetragonal Mn_3Ga thin films, *Phys. Rev. B* **87**, 18449 (2013).
- ²⁵ T. Hori, M. Akimitsu, H. Miki, K. Ohoyoama, and Y. Yamaguchi, Magnetic properties of $(\text{Mn}_{1-x}\text{Ru}_x)_3\text{Ga}$ alloys, *Appl. Phys. A* **74**, S737 (2002).
- ²⁶ H. Kurt, K. Rode, P. Stamenov, M. Venkatesan, Y.-C. Lau, E. Fonda, and J. M. D. Coey, Cubic

- Mn₂Ga thin films: crossing the spin gap with ruthenium, *Phys. Rev. Lett.* **112**, 027201 (2014).
- ²⁷ A. K. Nayak, M. Nicklas, S. Chadov, P. Khuntia, C. Shekhar, A. Kalache, M. Baenitz, Y. Skourski, V. K. Guduru, A. Puri, U. Zeitler, J. M. D. Coey, and C. Felser, Design of compensated ferrimagnetic Heusler alloys for giant tunable exchange bias, *Nature Mater.* **14**, 679 (2015).
- ²⁸ R. Sahoo, L. Wollmann, S. Selle, T. Höche, B. Ernst, A. Kalache, C. Shekhar, N. Kumar, S. Chadov, C. Felser, S. S. P. Parkin, and A. K. Nayak, Compensated ferrimagnetic tetragonal heusler thin films for antiferromagnetic spintronics, *Adv. Mater.* **28**, 8499 (2016).
- ²⁹ D. Betto, K. Rode, N. Thiyagarajah, Y.-C. Lau, K. Borisov, G. Atcheson, M. Zic, T. Archer, P. Stamenov, and J. M. D. Coey, The zero-moment half metal: How could it change spin electronics?, *AIP Advances* **6**, 055601 (2016).
- ³⁰ J. Finley and L. Liu, Spintronics with compensated ferrimagnets, *Appl. Phys. Lett.* **116**, 110501 (2020).
- ³¹ I. Galanakis, K. Özdoğan, E. Sasioglu, and S. Blügel, Effect of disorder on the magnetic properties of cubic Mn₂Ru_xGa compounds: A first-principles study, *J. Appl. Phys.* **116**, 033903 (2014).
- ³² M. Zic, K. Rode, N. Thiyagarajah, Y.-C. Lau, D. Betto, J. M. D. Coey, S. Sanvito, K. J. O'Shea, C. A. Ferguson, D. A. MacLaren, and T. Archer, Designing a fully compensated half-metallic ferrimagnet, *Phys. Rev. B* **93**, 140202 (2016).
- ³³ K. Fleischer, N. Thiyagarajah, Y.-C. Lau, D. Betto, K. Borisov, C. C. Smith, I. V. Shvets, J. M. D. Coey, and K. Rode, Magneto-optic Kerr effect in a spin-polarized zero-moment ferrimagnet, *Phys. Rev. B* **98**, 134445 (2018).
- ³⁴ K. E. Siewierska, G. Atcheson, A. Jha, K. Esien, R. Smith, S. Lenne, N. Teichert, J. O'Brien, J. M. D. Coey, P. Stamenov, and K. Rode, Magnetic order and magneto-transport in half-metallic ferrimagnetic Mn_yRu_xGa thin films, arXiv:2012.05736v4 (2021).
- ³⁵ S. Chatterjee, P. Dutta, P. Singha, S. Giri, A. Banerjee, and S. Majumda, Emergence of compensated ferrimagnetic state in Mn_{2-x}Ru_{1+x}Ga ($x = 0.2, 0.5$) alloys, *J. Magn. Magn. Mater.* **532**, 167956 (2021).
- ³⁶ S. Lenne, Y.-C. Lau, A. Jha, G. P. Y. Atcheson, R. E. Troncoso, A. Brataas, M. Hayashi, J. M. D. Coey, P. Stamenov, and K. Rode, Giant spin-orbit torque in a single ferrimagnetic metal layer, arXiv:1903.04432v1 (2019).
- ³⁷ C. Banerjee, N. Teichert, K. Siewierska, Z. Gercsi, G. Atcheson, P. Stamenov, K. Rode, J. M. D. Coey, and J. Besbas, Single pulse all-optical toggle switching of magnetization without

- gadolinium in the ferrimagnet $\text{Mn}_2\text{Ru}_x\text{Ga}$, *Nat. Commun.* **11**, 4444 (2020).
- ³⁸ G. P. Zhang, R. Meadows, A. Tamayo, Y. H. Bai, and T. F. George, An attempt to simulate laser-induced all-optical spin switching in a crystalline ferrimagnet, *AIP Adv.* **10**, 125323 (2020).
- ³⁹ C. Banerjee, K. Rode, G. Atcheson, S. Lenne, P. Stamenov, J. M. D. Coey, and J. Besbas, Ultrafast double pulse all-optical reswitching of a ferrimagnet, *Phys. Rev. Lett.* **126**, 177202 (2021).
- ⁴⁰ F. Jakobs and U. Atxitia, Atomistic spin model of single pulse toggle switching in $\text{Mn}_2\text{Ru}_x\text{Ga}$ Heusler alloys, arXiv:2106.10111v1.
- ⁴¹ G. P. Zhang, Y. H. Bai, and T. F. George, Switching ferromagnetic spins by an ultrafast laser pulse: Emergence of giant optical spin-orbit torque, *EPL* **115**, 57003 (2016).
- ⁴² G. Bonfiglio, K. Rode, G. Y. P. Atcheson, P. Stamenov, J. M. D. Coey, A. V. Kimel, Th. Rasing, and A. Kirilyuk, Sub-picosecond exchange-relaxation in the compensated ferrimagnet $\text{Mn}_2\text{Ru}_x\text{Ga}$, *J. Phys.: Condens. Matter* **33**, 135804 (2021).
- ⁴³ G. P. Zhang, M. Murakami, Y. H. Bai, T. F. George, and X. S. Wu, Spin-orbit torque-mediated spin-wave excitation as an alternative paradigm for femtomagnetism, *J. Appl. Phys.* **126**, 103906 (2019).
- ⁴⁴ G. P. Zhang, W. Hübner, E. Beaurepaire, and J.-Y. Bigot, Laser-induced ultrafast demagnetization: Femtomagnetism, A new frontier? *Topics Appl. Phys.* **83**, 245 (2002).
- ⁴⁵ A. Kirilyuk, A. V. Kimel, and Th. Rasing, Ultrafast optical manipulation of magnetic order, *Rev. Mod. Phys.* **82**, 2731 (2010). Erratum: *Rev. Mod. Phys.* **88**, 039904 (2016).
- ⁴⁶ L. Wollmann, S. Chadov, J. Kübler, and C. Felser, Magnetism in cubic manganese-rich Heusler compounds, *Phys. Rev. B* **90**, 214420 (2014).
- ⁴⁷ P. Blaha, K. Schwarz, G. K. H. Madsen, D. Kvasnicka, and J. Luitz, WIEN2k, An Augmented Plane Wave + Local Orbitals Program for Calculating Crystal Properties (Karlheinz Schwarz, Techn. Universität Wien, Austria, 2001).
- ⁴⁸ J. P. Perdew, K. Burke, and M. Ernzerhof, Generalized gradient approximation made simple, *Phys. Rev. Lett.* **77**, 3865 (1996).
- ⁴⁹ M. Hakimi, M. Venkatesan, K. Rode, K. Ackland, and J. M. D. Coey, The zero-magnetization Heusler ferrimagnet, *J. Appl. Phys.* **113**, 17B101 (2013).
- ⁵⁰ D. Betto, N. Thiyagarajah, Y.-C. Lau, C. Piamonteze, M.-A. Arrio, P. Stamenov, J. M. D. Coey, and K. Rode, Site-specific magnetism of half-metallic $\text{Mn}_2\text{Ru}_x\text{Ga}$ thin films determined

- by x-ray absorption spectroscopy, *Phys. Rev. B* **91**, 094410 (2015).
- ⁵¹ Supplementary Material contains additional information about the spin configuration and orbital-resolved band structures.
- ⁵² I. Radu, K. Vahaplar, C. Stamm, T. Kachel, N. Pontius, H. A. Dürr, T. A. Ostler, J. Barker, R. F. L. Evans, R. W. Chantrell, A. Tsukamoto, A. Itoh, A. Kirilyuk, Th. Rasing, and A. V. Kimel, Transient ferromagnetic-like state mediating ultrafast reversal of antiferromagnetically coupled spins, *Nature* **472**, 205 (2011).
- ⁵³ B. Koopmans, J. J. M. Ruigrok, F. Dalla Longa, and W. J. M. de Jonge, Unifying ultrafast magnetization dynamics, *Phys. Rev. Lett.* **95**, 267207 (2005).
- ⁵⁴ P. B. Allen, Electron Transport, *Conceptual foundations of Materials: A standard model for Ground- and Excited-State Properties*, Ed. S. Louie and M. Cohen (2006). Page 165.
- ⁵⁵ C. S. Wang and J. Callaway, Band structure of nickel: Spin-orbit coupling, the Fermi surface, and the optical conductivity, *Phys. Rev. B* **9**, 4897 (1975).
- ⁵⁶ P. M. Oppeneer, T. Maurer, J. Sticht, and J. Kübler, Ab initio Calculated magneto-optical Kerr effect of ferromagnetic metals: Fe and Ni, *Phys. Rev. B* **45**, 10924 (1992).
- ⁵⁷ M. Cazzaniga, L. Caramella, N. Manini and G. Onida, Ab initio intraband contributions to the optical properties of metals, *Phys. Rev. B* **82**, 035104 (2010).
- ⁵⁸ J. K. Dewhurst, P. Elliott, S. Shallcross, E. K. U. Gross, and S. Sharma, Laser-induced intersite spin transfer, *Nano Lett.* **18**, 1842 (2018).
- ⁵⁹ J. H. Mentink, J. Hellsvik, D. V. Afanasiev, B. A. Ivanov, A. Kirilyuk, A. V. Kimel, O. Eriksson, M. I. Katsnelson, and Th. Rasing, Ultrafast spin dynamics in multisublattice magnets, *Phys. Rev. Lett.* **108**, 057202 (2012).
- ⁶⁰ G. P. Zhang, Z. Babyak, Y. Xue, Y. H. Bai, and T. F. George, First-principles and model simulation of all-optical spin reversal, *Phys. Rev. B* **96**, 134407 (2017).
- ⁶¹ I. Galanakis, P. H. Dederichs, and N. Papanikolaou, Slater-Pauling behavior and origin of the half-metallicity of the full-Heusler alloys, *Phys. Rev. B* **66**, 174429 (2002).
- ⁶² W. B. Pearson, *The Crystal Chemistry and Physics of Metals and Alloys*, Wiley-Interscience, New York, London, Sydney, Toronto, (1958).
- ⁶³ Theo Hahn, *International Tables for Crystallography* (Dordrecht: Kluwer Academic Publishers, 2002).

TABLE I: Summary of the space group symmetries for X_2YZ used in the literature. Two X atoms are denoted as X_1 and X_2 , and “share” means that they share the same positions. For Mn_2RuGa , X_1 is Mn_1 , X_2 is Mn_2 , while Y is Ru and Z is Ga. The full-Heusler compound has $L2_1$ symmetry, the half-Heusler one has $C1_b$ symmetry, and the inverse Heusler compound has XA symmetry.

Group symmetry	Prototype	X_1	X_2	Y	Z	Ref.
$L2_1$ (No. 225, $Fm\bar{3}m$)	Cu_2MnAl	$8c(\frac{1}{4}, \frac{1}{4}, \frac{1}{4})$ share		$4b(\frac{1}{2}, \frac{1}{2}, \frac{1}{2})$	$4a(0, 0, 0)$	⁴⁶
$L2_1$ (No. 225, $Fm\bar{3}m$)		$(0, 0, 0)$	$(\frac{1}{2}, \frac{1}{2}, \frac{1}{2})$	$(\frac{1}{4}, \frac{1}{4}, \frac{1}{4})$	$(\frac{3}{4}, \frac{3}{4}, \frac{3}{4})$	⁶¹
$L2_1$ (No. 225, $Fm\bar{3}m$)	Cu_2MnAl	$8c(\frac{1}{4}, \frac{1}{4}, \frac{1}{4})$	$(\frac{3}{4}, \frac{3}{4}, \frac{3}{4})$	$4a(0, 0, 0)$	$4b(\frac{1}{2}, \frac{1}{2}, \frac{1}{2})$	⁶²
$C1_b$ (No. 216, $F\bar{4}3m$)	$MgAgAs$	$4a(0, 0, 0)$	vacant	$4b(\frac{1}{2}, \frac{1}{2}, \frac{1}{2})$	$4c(\frac{1}{4}, \frac{1}{4}, \frac{1}{4})$	⁶²
XA (No. 216, $F\bar{4}3m$)	Li_2AgSb	$4d(\frac{1}{4}, \frac{1}{4}, \frac{1}{4})$	$4b(\frac{1}{2}, \frac{1}{2}, \frac{1}{2})$	$4c(\frac{3}{4}, \frac{3}{4}, \frac{3}{4})$	$4a(0, 0, 0)$	⁴⁶
XA (No. 216, $F\bar{4}3m$)		$4a(0, 0, 0)$	$4c(\frac{3}{4}, \frac{3}{4}, \frac{3}{4})$	$4b(\frac{1}{2}, \frac{1}{2}, \frac{1}{2})$	$4d(\frac{1}{4}, \frac{1}{4}, \frac{1}{4})$	³¹
No. 216		$4a(0, 0, 0)$	$4c(\frac{1}{4}, \frac{1}{4}, \frac{1}{4})$	$4d(\frac{3}{4}, \frac{3}{4}, \frac{3}{4})$	$4b(\frac{1}{2}, \frac{1}{2}, \frac{1}{2})$	⁶³

TABLE II: Spin and orbital moments of Mn_1 , Mn_2 , Ru and Ga. The electron populations in their majority and minority $3d$ states are listed as $n_{3d,\uparrow}$ and $n_{3d,\downarrow}$. The demagnetization rate in regions I and II is denoted as α^I and α^{II} , respectively. In two artificial structures, Mn_2Ru and Mn_2Ga , only the spin moments are given.

Element	$M_s(\mu_B)$	$M_o(\mu_B)$	$n_{3d\uparrow}$	$n_{3d\downarrow}$	$\alpha^I(1/ps)$	$\alpha^{II}(1/ps)$	$M_s(\mu_B)$	$M_s(\mu_B)$
	(Mn ₂ RuGa)						(Mn ₂ Ru)	(Mn ₂ Ga)
$Mn_1(4a)$	3.17	0.025	4.09	1.01	4.5	0.6	2.80	3.35
$Mn_2(4c)$	-2.31	-0.046	1.44	3.72	2.8	1.5	-3.64	-3.27
$Ru(4d)$	0.076	-0.035					-0.39	NA
$Ga(4b)$	0.032	-0.000					NA	-0.04

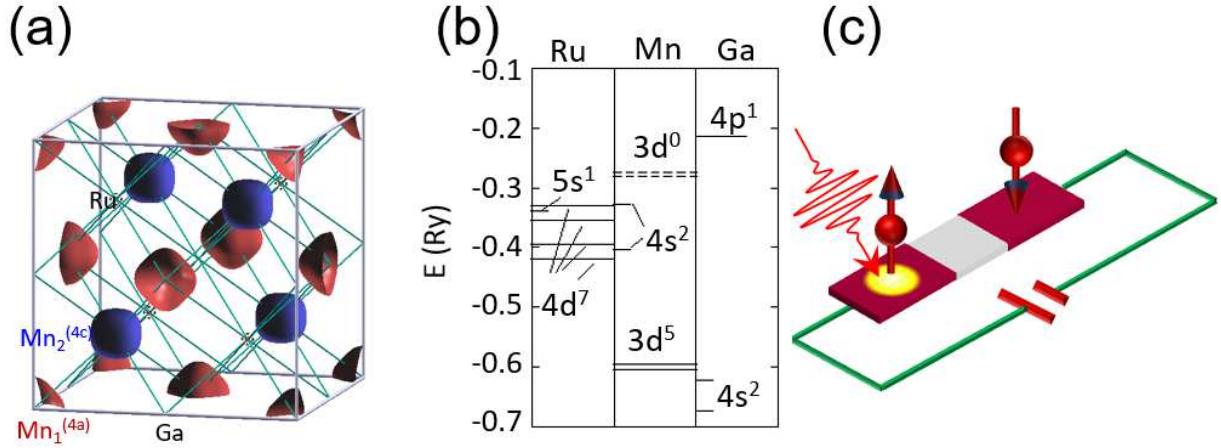


FIG. 1: (a) Structure of Mn₂RuGa and the spatial spin densities on the Mn₁(4a) (red, positive) and Mn₂(4c) (blue, negative). The Ru and Ga atoms have a small spin density. (b) Atomic energy levels of Ru, Mn and Ga. The energy splitting is due to the spin-orbit coupling in atoms. (c) Our proposed device has a junction structure and consists of three layers of the same Mn₂Ru_xGa, but with different composition x . The layer on the left is an optically active layer, the middle is the spin filter, and the right layer is a spin reference layer. The magnetoresistance is controlled by light.

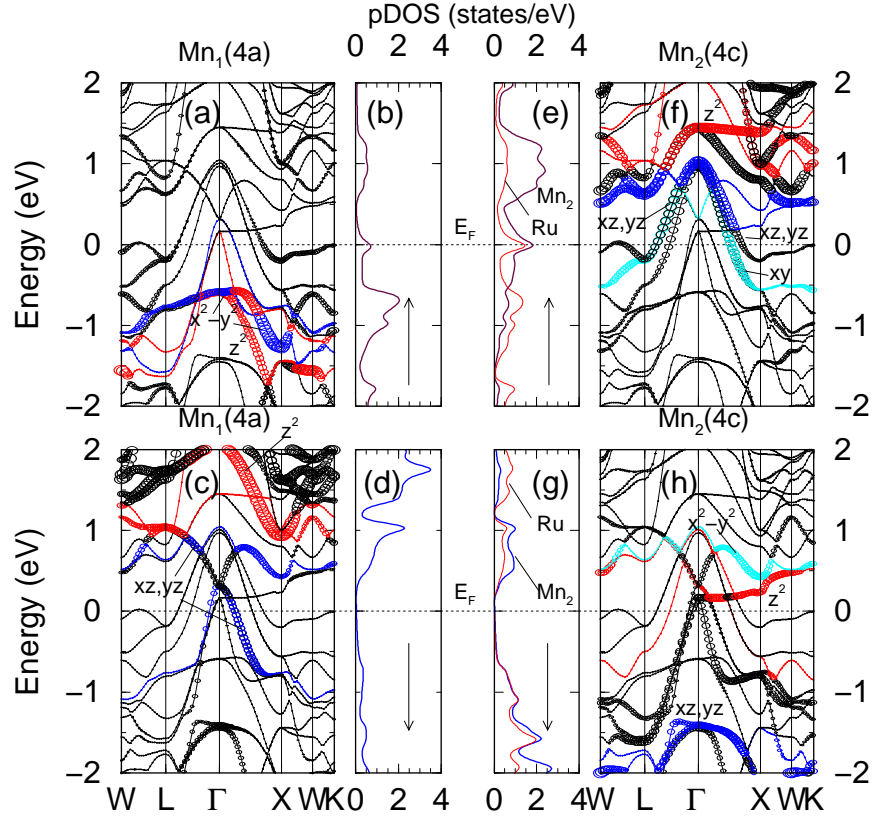


FIG. 2: (a) and (c) Orbital-resolved band structure with the 3d state characters for the $\text{Mn}_1(4a)$ spin-majority and spin-minority channels, respectively. (b) and (d) Partial density of states for the Mn_1 spin-majority and spin-minority channels, respectively. Bands with clear orbital characters are denoted by their orbitals. The Fermi level is set at 0 eV (horizontal dashed line). (f) and (h) Band structure with the 3d state characters for the $\text{Mn}_2(4c)$ spin-majority and spin-minority channels, respectively. (e) and (g) Partial density of states for the Mn_2 's 3d (thick lines) and Ru's 4d (thin lines) spin-majority and spin-minority, respectively.

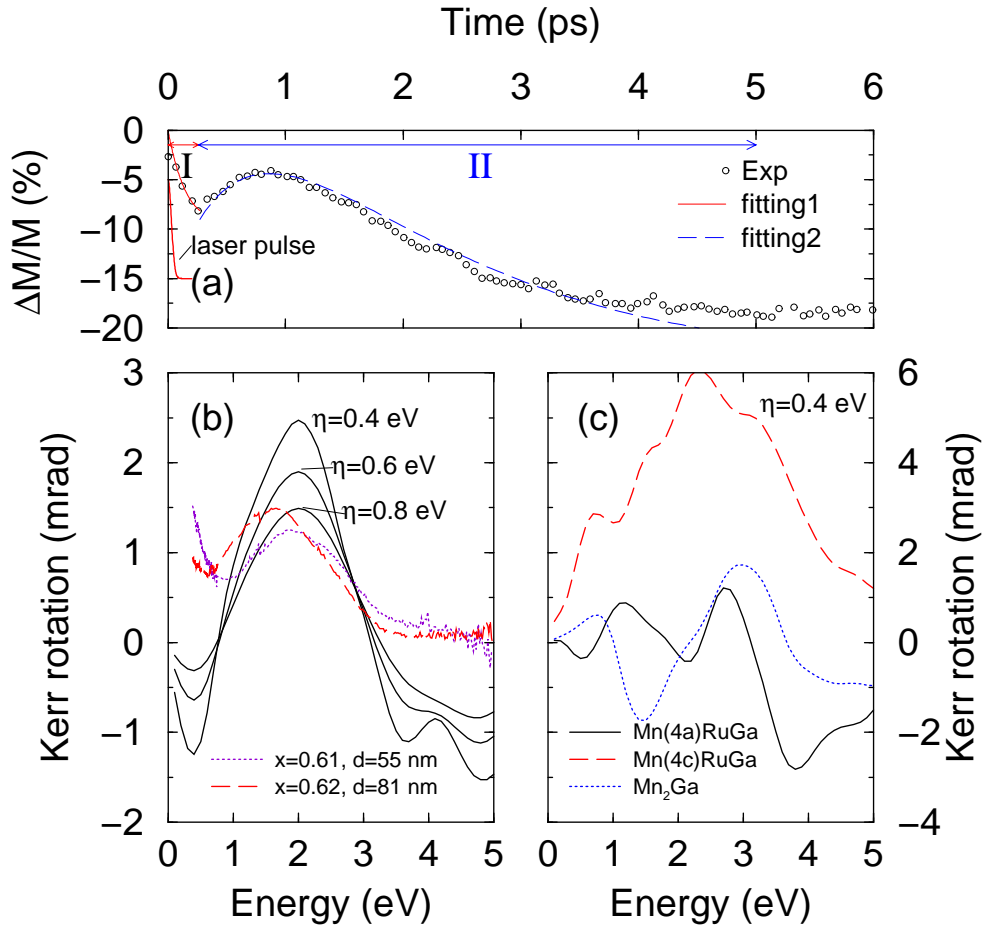


FIG. 3: (a) Experimental demagnetization fitted by Eq. 2, with two sets of fitting parameters given in Table II, provides a crucial insight that demagnetization rates at two Mn spin-sublattices change between region I (between 0 to 0.26 ps) and region II (between 0.26 ps to 5 ps). The experimental data are extracted from Ref.⁴². The thick red curve is the laser pulse of duration 40 fs. (b) The experimental (dotted and dashed lines from Ref.³³) and our theoretical Kerr rotation angles. The three solid lines are our theoretical results with three different dampings $\eta = 0.4, 0.6, 0.8$ eV. (c) Element-resolved Kerr rotation angles when Mn₂(4c) (solid line), or Mn₁(4a) (dashed line), or Ru (dotted line) is removed separately. $\eta = 0.4$ eV is used.